



# Highly active Co–B amorphous alloy catalyst with uniform nanoparticles prepared in oil-in-water microemulsion

Hui Li<sup>a</sup>, Jun Liu<sup>a</sup>, Songhai Xie<sup>b</sup>, Minghua Qiao<sup>b</sup>, Weilin Dai<sup>b</sup>, Hexing Li<sup>a,\*</sup>

<sup>a</sup> Department of Chemistry, Shanghai Normal University, Shanghai 200234, PR China

<sup>b</sup> Department of Chemistry, Fudan University, Shanghai 200433, PR China

## ARTICLE INFO

### Article history:

Received 29 March 2008

Revised 28 July 2008

Accepted 29 July 2008

Available online 23 August 2008

### Keywords:

Co–B amorphous alloy catalyst

Uniform diameter

Microemulsion

Cinnamaldehyde

Hydrogenation

Cinnamyl alcohol

## ABSTRACT

Uniform Co–B nanoparticles were synthesized for the first time by chemical reduction of cobalt ion with borohydride in an oil-in-water microemulsion system comprising cyclohexane, polyethylene glycol, and water. The particle size was controlled by modulating the cyclohexane content. With the characterization of X-ray diffraction, selective area electronic diffraction, X-ray photoelectron spectroscopy, and transmission electron microscopy, the resulting Co–B nanoparticles were identified to be amorphous alloys ranging in size from 6 to 20 nm. During liquid-phase cinnamaldehyde hydrogenation, the as-synthesized Co–B catalyst was extremely active and more selective than the regular Co–B prepared in aqueous solution. Furthermore, this catalyst also was found to be more durable during the hydrogenation process.

© 2008 Elsevier Inc. All rights reserved.

## 1. Introduction

The hydrogenation of cinnamaldehyde (CMA) to cinnamyl alcohol (CMO) is widely applied in the production of perfumes, flavorings, pharmaceuticals, and other fine chemicals [1]. Up to now, only the Ir-, Os-, and Pt-based catalysts have been used to achieve high selectivity to CMO, because hydrogenation of C=C is always easier than hydrogenation of C=O [2–6]. However, the high cost and nonavailability of these catalysts pose a problem. Co-based catalysts are more selective toward CMO compared with other nonnoble metal catalysts [7], but their practical applications remain limited due to their very low activity. Amorphous alloys (metallic glasses), metastable materials with long-range disordered but short-range ordered structure, have attracted growing attention from both academia and industry due to their superior corrosion resistance, high mechanical toughness, and excellent magnetic, electronic, and catalytic properties compared with their crystalline counterparts [8]. As heterogeneous catalysts, amorphous alloys have been widely studied because of their excellent catalytic performances [8–11]. To form and stabilize the amorphous structure, some metalloids (e.g., B) should be incorporated in amorphous alloys, significantly affecting their physical and chemical properties [12,13]. The synthesis of ultrafine particles through chemical reduction has been most often used to prepare these

kinds of M–B amorphous alloy catalysts [12,13]. But vigorous and exothermic reactions between metallic ions and borohydride ( $\text{BH}_4^-$ ) usually induce particle aggregation, thereby reducing catalytic activity because of the low surface area in the catalysts. Meanwhile, the nonuniform nanoparticles also are responsible for the ready crystallization of amorphous alloys [14]. Although monodispersed nanostructured metal colloids have been reported [15], few attempts have been made to prepare M–B amorphous alloy in uniform nanoparticles, possibly because the reduction of metallic ions by  $\text{BH}_4^-$  is uncontrollable and strongly exothermic in preparation. Previously, we reported a Co–B amorphous alloy catalyst with uniform particle size prepared by ultrasound-assisted reduction of  $\text{Co}(\text{NH}_3)_6^{2+}$  with  $\text{BH}_4^-$  in aqueous solution [14]. But the slow reduction process resulted in relatively large (>50 nm) Co–B particles unfavorable for catalytic activity.

Recently, size-and-morphology control synthesis of nanoparticles has been achieved through reverse microemulsion [16–18]. A series of Ni–B amorphous alloy catalysts were successfully synthesized in a water-in-oil microemulsion system [19]. But using large amounts of organic phase in microemulsions may cause several problems, including low concentration of products, difficult separation, and even environmental pollution [20]. Thus, there is a great need to design simple methods that can produce large quantities of uniform nanoparticles in a desired size range.

In this paper, we report the synthesis of uniform Co–B amorphous alloy nanoparticles by conducting the chemical reduction of  $\text{Co}^{2+}$  with  $\text{BH}_4^-$  in an oil-in-water microemulsion system. The nanoparticles could be easily collected and the particle size freely

\* Corresponding author. Fax: +86 21 64322272.

E-mail address: hexing-li@shnu.edu.cn (H. Li).

adjusted by changing the amount of oil phase in the microemulsion. During liquid-phase hydrogenation of CMA to CMO, the as-prepared Co–B exhibited better catalytic performance (activity, selectivity, and durability) than the Co–B prepared by direct reduction of  $\text{Co}^{2+}$  with  $\text{BH}_4^-$  or even by ultrasound-assisted reduction of  $\text{Co}(\text{NH}_3)_6^{2+}$  with  $\text{BH}_4^-$ . The correlation of the catalytic performances to the structural properties has been tentatively established.

## 2. Experimental

### 2.1. Catalyst preparation

In a typical run of catalyst synthesis,  $\text{CoCl}_2 \cdot 6\text{H}_2\text{O}$  (5.0 mmol, 1.2 g) and polyethylene glycol ( $M_w = 20,000$ , 5.0 g) were first dissolved in deionized water (40 ml), then an appropriate amount of cyclohexane was added to this solution. The mixture thus obtained was treated under ultrasonic radiation at 293 K for 30 min, with an oil-in-water microemulsion formed. Then a 2.0 M  $\text{KBH}_4$  aqueous solution (10 ml) was added dropwise under vigorous stirring at 293 K. After reaction was complete, the black precipitate was washed free from  $\text{Cl}^-$  or  $\text{K}^+$  ions with deionized water until a pH  $\sim 7$  was achieved, followed by three washings with absolute alcohol (EtOH). Finally, the mixture was stored in EtOH until use. The as-prepared Co–B samples were designated Co–B- $x$ , with  $x$  representing the volume ratio of cyclohexane to water. The direct reduction of  $\text{CoCl}_2$  with  $\text{KBH}_4$  in pure aqueous solution resulted in the regular Co–B sample [21] and was designated Co–B-0. The Co–B-50-30 was prepared by ultrasound-assisted reduction of  $\text{Co}(\text{NH}_3)_6^{2+}$  with  $\text{BH}_4^-$  in aqueous solution [14], where 50 and 30 refer to the ultrasound power (W) and ultrasonication time (min), respectively.

### 2.2. Characterization

The bulk composition was analyzed by inductively coupled plasma optical emission (ICP; Varian VISTA-MPX). The amorphous structure was determined by both X-ray diffraction (XRD; Rigaku D/Max-RB with  $\text{CuK}\alpha$  radiation) and electivity area electronic diffraction (SAED; JEOL JEM-2010). Surface morphology and particle size were observed by transmission electron microscopy (TEM; JEOL JEM2010). The size distribution was evaluated from about 300 randomly selected particles. Thermal stability was determined by differential scanning calorimetry (DSC; Shimadzu DSC-60) under  $\text{N}_2$  atmosphere, at a heating rate of  $10 \text{ Kmin}^{-1}$ . The active surface area ( $S_{\text{Co}}$ ) was measured by hydrogen chemisorption on a Quantachrome CHEMBET 3000 system, assuming  $\text{H}/\text{Co}(s) = 1$  and a surface area of  $6.5 \times 10^{-20} \text{ m}^2$  per Co atom [22]. The hydrogen temperature-programmed desorption ( $\text{H}_2$ -TPD) curves were obtained on the same instrument in argon flow at a ramping rate of  $20 \text{ Kmin}^{-1}$ . The surface electronic states were investigated by X-ray photoelectron spectroscopy (XPS; Perkin-Elmer PHI 5000C ESCA using  $\text{AlK}\alpha$  radiation), and all Co–B samples were dried in pure Ar atmosphere before measurements. The binding energy (BE) values were calibrated using  $\text{C } 1s = 284.6 \text{ eV}$  as a reference.

### 2.3. Activity test

Liquid-phase hydrogenation of CMA was carried out in a 200-ml stainless autoclave containing 0.30 g of catalyst, 4 ml of CMA, 40 ml of EtOH, and 1.0 MPa of  $\text{H}_2$  at 373 K. The reaction system was stirred vigorously (1000 rpm) to eliminate the diffusion effects [23]. According to the  $P_{\text{H}_2}$  drop with the reaction time, both the specific activity [i.e.,  $\text{H}_2$  uptake rate per gram of cobalt,  $R_{\text{H}}^{\text{m}}$  ( $\text{mmol h}^{-1} \text{g}_{\text{Co}}^{-1}$ )] and the areal activity [i.e.,  $\text{H}_2$  uptake rate per  $\text{m}^2$  of the active surface area,  $R_{\text{H}}^{\text{S}}$  ( $\text{mmol h}^{-1} \text{m}_{\text{Co}}^{-2}$ )] were calculated

using the ideal gas equation. The  $R_{\text{H}}^{\text{S}}$  should represent the intrinsic activity, because the effect of metal dispersion has been ruled out. During the reaction, samples were withdrawn from the reaction mixture every 30 min for product analysis using a gas chromatograph (GC 102) with a flame ionization detector. The stationary phase was 15% Apiezon (L)/Gas Chrom (red) at 523 K with  $\text{N}_2$  as carrier gas. All results have been reproduced, and the errors were limited within  $\pm 5\%$ .

## 3. Results and discussion

### 3.1. Structural and electronic characteristics

The TEM images (Fig. 1a) show that Co–B-0 displayed irregular, broadly dispersed particles, apparently due to the particle agglomeration, because the reaction between  $\text{Co}^{2+}$  and  $\text{BH}_4^-$  is strongly exothermic [12]. In contrast, the Co–B nanoparticles synthesized in an oil-in-water microemulsion were spherical and relatively uniform, and the particle size decreased from 20 to 6 nm as the cyclohexane/water volume ratio was increased from 0.1 to 0.25 (Figs. 1b–1d), which was obviously much smaller than the Co–B-50-30 synthesized through ultrasound-assisted reduction of  $\text{Co}(\text{NH}_3)_6^{2+}$  with  $\text{BH}_4^-$  [14]. The relatively narrow distribution for the as-prepared nanoparticles can be attributed mainly to the dispersing effect of oil droplets in microemulsion, which can restrict particle growth and even prevent aggregation of the Co–B nanoparticles. An increase in the cyclohexane content may enhance the dispersing effect, leading to decreased particle size (Figs. 1b–1d); however, a further increase in the amount of cyclohexane could induce significant agglomeration due to the extremely high surface energy in small Co–B nanoparticles (Fig. 1e).

ICP analysis revealed that the bulk compositions in all Co–B- $x$  samples were very close (Table 1). The higher B content in Co–B- $x$  compared with in Co–B-0 may be due to the inhibition of  $\text{BH}_4^-$  hydrolysis in the microemulsion, which would enhance the activity of the reaction solution and the formation of B-enriched amorphous alloys [24]. Table 1 also shows that the  $S_{\text{Co}}$  of Co–B- $x$  samples initially increased and then decreased with increasing cyclohexane content in the microemulsion. The maximum  $S_{\text{Co}}$  was obtained for Co–B-0.25, obviously due to the smallest particle size (see Fig. 1). Co–B-50-30 displayed a higher  $S_{\text{Co}}$  than Co–B-0, due to the ultrasound effect, which can clean the catalyst surface and also inhibit the particle agglomeration. Co–B-0.25 showed even higher  $S_{\text{Co}}$  than Co–B-50-30, obviously due to its smaller particle size. The XRD patterns presented in Fig. 2 show that, similar to the Co–B-0 and Co–B-50-30 [14], all Co–B samples synthesized in oil-in-water microemulsion (e.g. Co–B-0.25) exhibited a single broad peak around  $2\theta = 45^\circ$  indicative of amorphous structure [25], which can be further confirmed by a successive diffraction halo in an attached SAED image [26]. Treatment of the fresh Co–B-0.25 sample (at 673 K in  $\text{N}_2$  for 2 h) resulted in the appearance of various diffraction peaks corresponding to metallic Co and crystalline Co–B alloy. The appearance of Co–B crystalline phases during the crystallization process verified the formation of an alloy between Co and B for the as-prepared Co–B. In addition, our previous work also demonstrated the presence of Co–B bond through EXAFS analysis [21]. The presence of a shoulder peak at around 1.7 Å at the radial distribution functions obtained from the  $\text{Co } \chi(k)k^3$  edge by fast Fourier transformation suggests the formation of a Co–B bond. Furthermore, calculations based on the EXAFS reveal that the Co–B bond length was much shorter than the sum of Co radius and B radius, which also suggests the formation of Co–B alloy. We infer that except for the crystallization, partial decomposition of a Co–B amorphous alloy may occur in this process. The DSC analysis (Fig. 3) reveals that the crystallization of the Co–B-0 sample involved two steps: rearrangement of Co–B amorphous

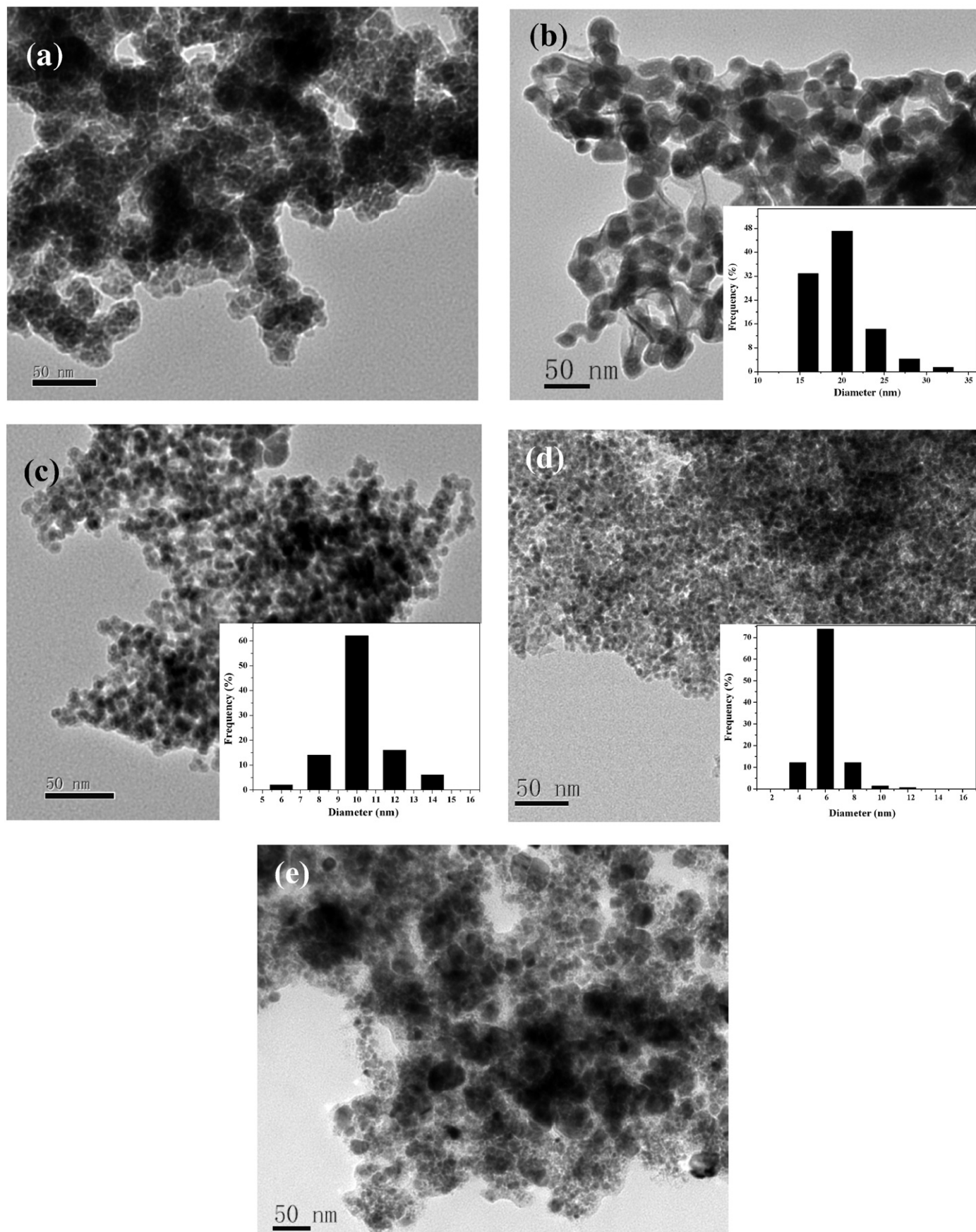


**Fig. 1.** TEM morphologies and their corresponding size distribution histograms (inserts) of the fresh Co-B samples. (a) Co-B-0, (b) Co-B-0.1, (c) Co-B-0.2, (d) Co-B-0.25, and (e) Co-B-0.3.

**Table 1**  
Structural properties and catalytic performances of the as-prepared catalysts<sup>a</sup>

| Catalyst                | Composition (at%)                    | $S_{\text{Co}}$ ( $\text{m}^2 \text{g}^{-1}$ ) | $R_{\text{H}}^{\text{m}}$ ( $\text{mmol h}^{-1} \text{g}_{\text{Co}}^{-1}$ ) | $R_{\text{H}}^{\text{S}}$ ( $\text{mmol h}^{-1} \text{m}_{\text{Co}}^{-2}$ ) | Time <sup>b</sup> (h) | Yield <sup>b</sup> (%) |
|-------------------------|--------------------------------------|--|--|--|-----------------------|------------------------|
| Co-B-0                  | Co <sub>75.4</sub> B <sub>24.6</sub> | 15.8   | 19.5   | 1.2  | 8.0                   | 80.3                   |
| Co-B-0.1                | Co <sub>60.2</sub> B <sub>39.8</sub> | 13.6   | 20.4   | 1.5  | 9.0                   | 80.0                   |
| Co-B-0.2                | Co <sub>62.5</sub> B <sub>37.5</sub> | 36.9   | 57.0   | 1.5  | 4.0                   | 81.6                   |
| Co-B-0.25               | Co <sub>61.9</sub> B <sub>38.2</sub> | 42.6   | 69.9   | 1.6  | 3.5                   | 85.6                   |
| Co-B-0.3                | Co <sub>59.7</sub> B <sub>40.3</sub> | 32.2   | 48.3   | 1.5  | 4.0                   | 74.3                   |
| Crystallized            |                                      |  |  |  |                       |                        |
| Co-B-0.25 <sup>c</sup>  | Co <sub>61.9</sub> B <sub>38.2</sub> | 12.6   | 11.5   | 0.9  | 10.0                  | 68.5                   |
| Co-B-50-30 <sup>d</sup> | Co <sub>77.7</sub> B <sub>22.3</sub> | 25.5   | 34.7   | 1.4  | 4.5                   | 80.0                   |

<sup>a</sup> Reaction conditions: catalyst containing 0.3 g Co, 4 ml of CMA, 40 ml of EtOH,  $T = 373 \text{ K}$ ,  $P_{\text{H}_2} = 1.0 \text{ MPa}$ , stirring rate = 1000 rpm.

<sup>b</sup> Values corresponding to the maximum CMO yield.

<sup>c</sup> Obtained by treating Co-B-0.25 amorphous alloy at 673 K for 2 h in  $\text{N}_2$ .

<sup>d</sup> Prepared via reduction of  $\text{Co}(\text{NH}_3)_6^{2+}$  with  $\text{BH}_4^-$  with ultrasound power of 50 W and 30 min [14].

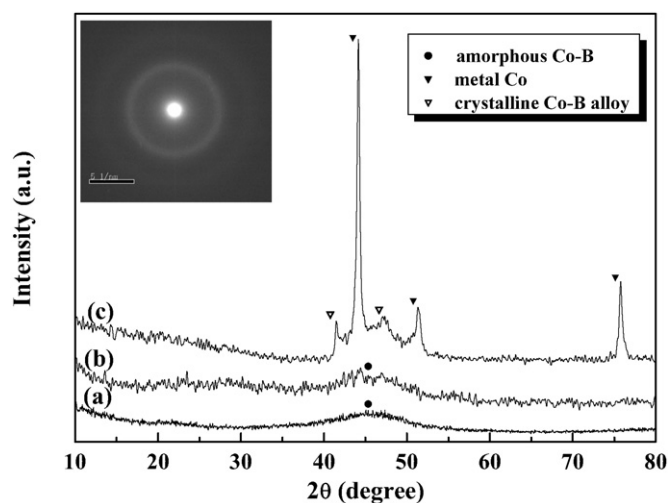


**Fig. 2.** XRD patterns of (a) the fresh Co-B-0, (b) the fresh Co-B-0.25, and (c) the Co-B-0.25 sample after being treated at 673 K for 2 h in  $\text{N}_2$  flow. The insert is the SAED image of the fresh Co-B-0.25 sample.

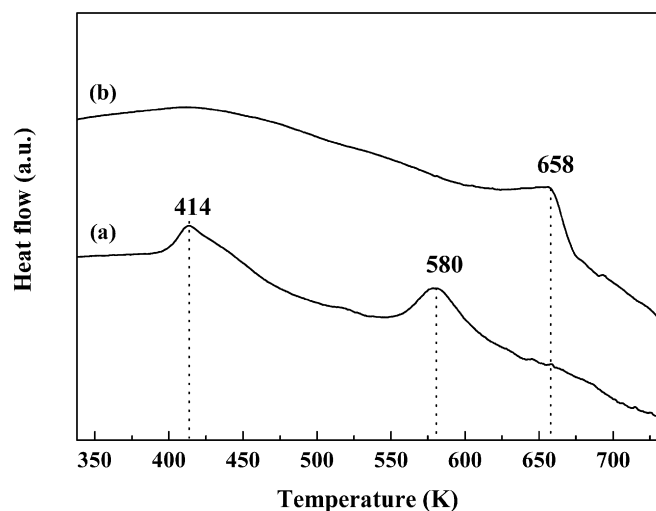


**Fig. 3.** DSC curves of (a) Co-B-0, and (b) Co-B-0.25 samples.

alloy structure and the crystallization of Co-B amorphous alloy with exothermic peaks at around 414 and 580 K [21]. But Co-B-0.25 displayed only one exothermic peak at 658 K, higher than that for Co-B-0 by 78 K. Obviously, the as-prepared Co-B- $x$  samples exhibited much stronger thermal stability against crystallization than Co-B-0. The enhanced thermal stability is obviously related to the

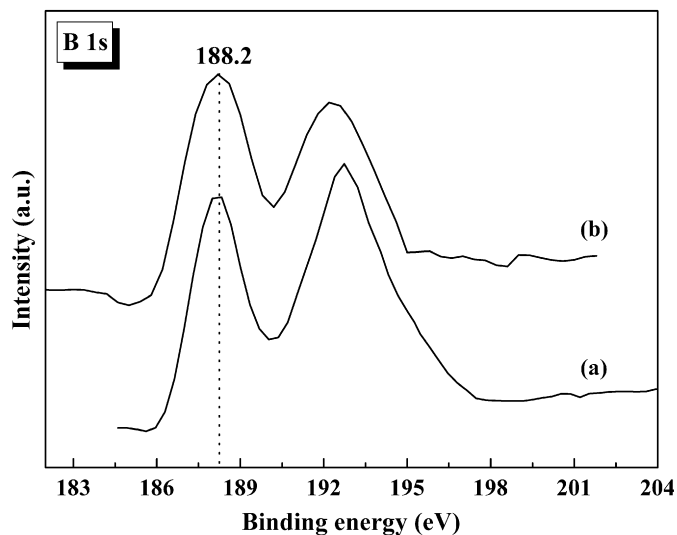
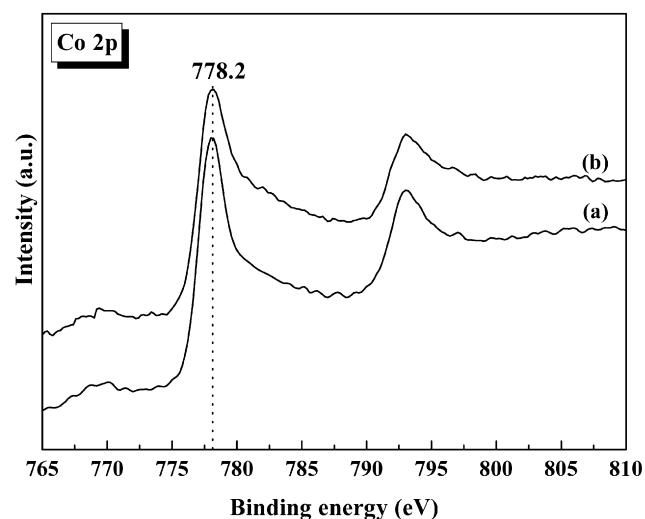
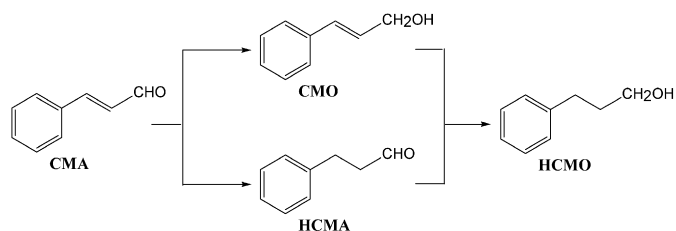


**Fig. 4.** XPS spectra of (a) Co-B-0, and (b) Co-B-0.25 samples.

increased B content in Co-B alloys [24]. On the other hand, the uniform particle size may inhibit the particle migration and agglomeration, a key step in the crystallization process [27]. The XPS spectra (Fig. 4) revealed that for all Co species in either Co-B-0 or Co-B-0.25, the core level of  $\text{Co } 2p_{3/2}$  was at 778.2 eV, indicating that all Co atoms were present in metallic state [28]. But the B species were present in both the elemental B and the oxidized B, with B1s BE values of around 188.2 and 192.5 eV. The B1s BE of



Scheme 1. Possible reaction pathways for CMA hydrogenation.

the elemental B in Co–B-0.25 exceeded that of pure B (187.1 eV) by 1.1 eV [29], further indicating that the elemental B is alloyed with the metallic Co. In alloys, partial electrons may be transferred from B to Co, as has been detected in a Co–B-0 sample [21] and demonstrated by a theoretic calculation based on the  $\text{Co}_m\text{B}_2$  ( $m = 1-4$ ) cluster models using density functional theory [30]. This also was confirmed by the finding that the metal in the M–B amorphous alloy had a much stronger antioxidation ability than the pure metal, due to the presence of electron-deficient B that could effectively protect the metal from oxidation [31]. The failure in observing the BE shift of the metallic Co can be understood by considering its relatively greater atomic weight compared with the B atom [29]. Thus, considering the results from XRD, SAED, DSC, and XPS, we can conclude that Co–B amorphous alloy was formed through the present method. According to the calculation based on XPS peak areas, the surface molar ratio of the alloying B to the metallic Co in Co–B-0.25 was 38/62, higher than that in either Co–B-0 (28/72) or even in Co–B-50-30 (32/68) [14], implying that Co–B-0.25 was surface-enriched with the alloying B [24].

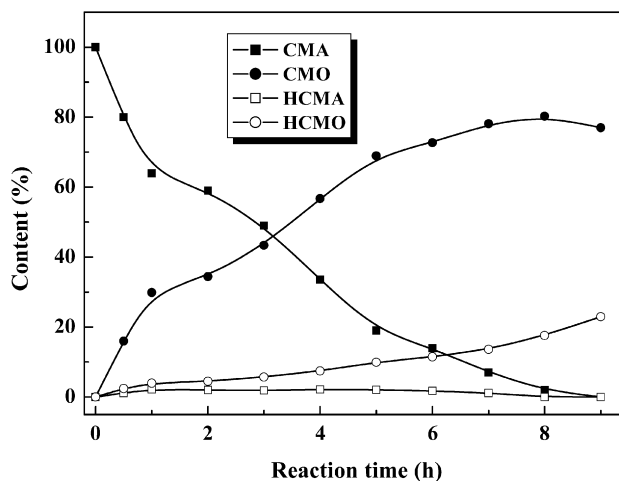
### 3.2. Catalytic performance

Fig. 5 shows the changes of solution composition with reaction time during CMA hydrogenation over the Co–B-0 and Co–B-0.25 samples. Along with the production of CMO, dihydrocinnamaldehyde (HCMA) and 3-phenylpropanol (HCMO) were identified as two byproducts. The CMA hydrogenation process is illustrated in Scheme 1 [1]. The main product CMO is produced from the selective hydrogenation of the C=O bond in CMA. The competitive hydrogenation of C=C against C=O in CMA results in the formation of HCMA. HCMO is produced by further hydrogenation of either CMO or HCMA.

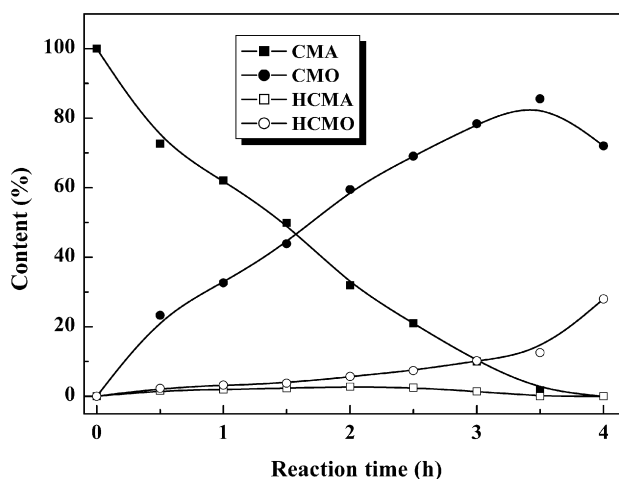
We compared the catalytic efficiencies of Co–B-0.25 and Co–B-0 amorphous catalysts and several conventionally synthesized Co-based catalysts, including Co/SiO<sub>2</sub> [32], Co/Al<sub>2</sub>O<sub>3</sub> [33], and Raney Co [34]. As shown in Fig. 6, the as-prepared Co–B amorphous alloys exhibited much greater CMO yields compared with the Co-based catalysts reported previously. The superior catalytic properties of the as-prepared catalysts can be attributed to their unique short-range ordering, whereas a long-range disordering amorphous structure has proven favorable for hydrogenation processes [8–13]. This is supported by the fact that fresh Co–B-0.25 exhibited much higher activity and selectivity to CMO than the corresponding crystallized catalyst obtained by treating the fresh catalyst at 673 K for 2 h in N<sub>2</sub> flow (see Table 1). The superior performance of the Co–B amorphous alloy catalyst over its corresponding crystalline catalyst can be interpreted in terms of both structural and the electronic effects.

#### 3.2.1. Structural effect

According to our previous EXAFS analysis [23], the Co–B amorphous alloy displayed a shorter Co–Co bonding length ( $R_{\text{Co-Co}}$ ), a lower coordination number ( $N$ ) of Co–Co first neighboring shell, and a higher DW factor ( $\sigma$ ) than the crystalline catalysts (Table 2). The  $R_{\text{Co-Co}}$  represented stronger synergistic effect between



(a)



(b)

Fig. 5. Reaction profiles of CMA hydrogenation over (a) Co–B-0, and (b) Co–B-0.25 samples. Reaction conditions are given in Table 1.

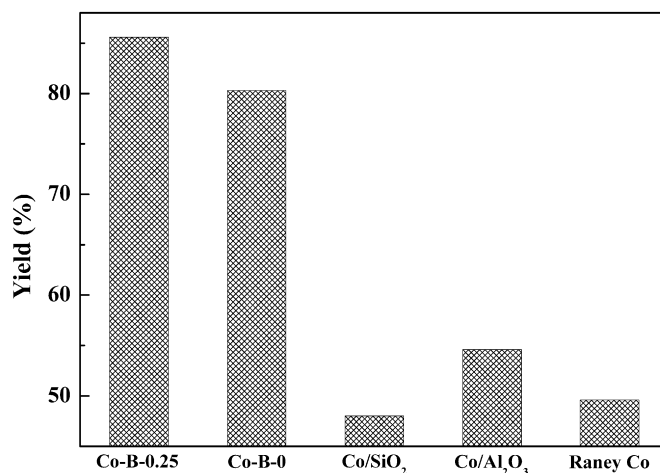
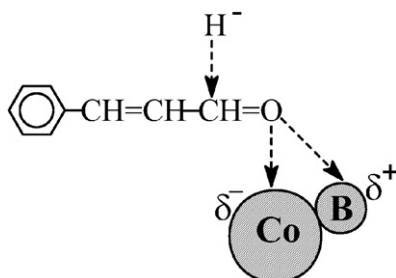


Fig. 6. CMO yield obtained on Co–B-0.25, Co–B-0, Co/SiO<sub>2</sub>, Co/Al<sub>2</sub>O<sub>3</sub>, and Raney Co catalysts.

Co active sites, and the lower  $N$  corresponded to more highly unsaturated Co active sites, which may promote the adsorption of reactant molecules and the surface hydrogenation [35]. Meanwhile, the higher  $\sigma$  implies a more homogeneous distribution of Co active sites, and the uniform Co active sites are beneficial for the selectivity to CMO [32].

**Table 2**  
Structural parameters of Co-based samples calculated from EXAFS analysis

| Sample               | $R_{\text{Co-Co}}$<br>(Å) | Coordination<br>number ( $N$ ) | DW factor<br>$\sigma$ (nm) |
|----------------------|---------------------------|--------------------------------|----------------------------|
| Co-B amorphous alloy | 2.42                      | 8.7                            | 0.0248                     |
| Crystallized Co-B    | 2.55                      | 10.6                           | 0.0212                     |
| Raney Co             | 2.51                      | 9.9                            | 0.0226                     |



**Scheme 2.** A plausible model of CMA adsorption and hydrogenation on Co-B amorphous alloy.

### 3.2.2. Electronic effect

Blyholder et al. [36] confirmed that a metal–oxygen bond, rather than a metal–carbon bond, was responsible for the bonding between the carbonyl group and Co metal. Noller et al. [37] also confirmed that the C=O hydrogenation started with the attack of  $\text{H}^-$  on the C atom. The aforementioned XPS spectra demonstrated the strong electronic interaction between Co and B in the Co-B amorphous alloy, making Co electron-enriched but making B electron-deficient. On one hand, the higher electron density on Co active sites could facilitate the formation of  $\text{H}^-$  species [37], possibly promoting CMA hydrogenation. On the other hand, the electron-enriched Co active sites were favorable for activating the adsorbed C=O group through an electron back-donation from  $d_{x^2-y^2}$  orbital of Co to the  $\pi_{\text{C=O}}^*$  antibonding orbital of the C=O group, leading to the enhanced hydrogenation activity [38]. Meanwhile, the electron-enriched Co active sites could effectively inhibit the adsorption of C=C bond due to the presence of a benzene ring, which also is electron-enriched, which could retard the hydrogenation of C=C bond, leading to the enhanced selectivity to CMO. Furthermore, the electron-deficient B could strengthen the adsorption for C=O group through a side-bond interaction (Scheme 2), activating the C=O bond toward hydrogenation [39]. But no electron donation-acceptance was present in the Co-based crystalline catalysts, which could account for the lower activity and selectivity to CMO compared with the corresponding Co-B amorphous alloy catalysts [40]. The XPS spectra revealed that all Co species were present in the metallic state. Nevertheless, both the elemental B and the oxidized B were detected in all of the as-prepared Co-B samples. Thus, the presence of oxygen is related to boron oxide.

To investigate the effect of boron oxide on the catalytic properties of Co active sites, we prepared pure Co and Co/B<sub>2</sub>O<sub>3</sub> catalysts by chemical reduction of Co<sup>2+</sup> and Co<sup>2+</sup>/B<sub>2</sub>O<sub>3</sub> precursor with NH<sub>2</sub>NH<sub>2</sub> alkaline solution at 363 K and conducted CMA hydrogenation over these catalysts under the same reaction conditions as specified in Table 1. The control experiments reveal that pure Co and Co/B<sub>2</sub>O<sub>3</sub> catalysts had similar hydrogenation processes and catalytic properties. After reaction for 12 h, the maximum CMO yield was obtained as 25.6% and 27.3%, respectively. Apparently, all of the Co-B amorphous alloy catalysts had much better catalytic properties than the pure Co and Co/B<sub>2</sub>O<sub>3</sub> catalysts. Therefore, the influence of boron oxide on the catalytic properties of Co-B amorphous was insignificant compared with the B alloying with Co.

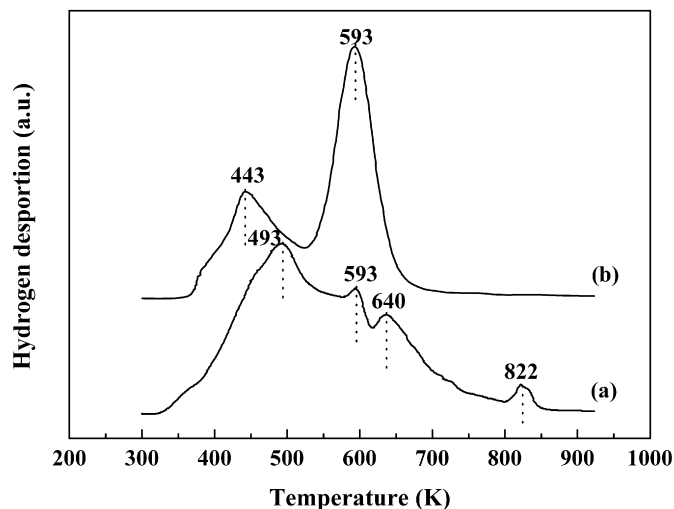


**Fig. 7.** Hydrogen TPD curves of (a) Co-B-0, and (b) Co-B-0.25 samples.

Table 1 also revealed that Co-B-0.25 exhibited much higher  $R_{\text{H}}^{\text{m}}$  and shorter time to obtain optimum CMO yield than Co-B-0. This may be attributed to both the larger metallic area ( $S_{\text{Co}}$ ) and the enhanced intrinsic activity ( $R_{\text{H}}^{\text{S}}$ ). As demonstrated by the XPS results, Co-B-0.25 has a higher B content than Co-B-0, which can account for the higher  $R_{\text{H}}^{\text{S}}$  from Co-B-0.25 compared with Co-B-0. On one hand, the Co in Co-B-0.25 was more electron-enriched than Co-B-0, due to the electron back-donation from B [29], which resulted in enhanced catalytic activity as discussed above. Co-B-0.25's greater CMO yield made it more selective than Co-B-0, due to the uniform Co-B nanoparticles [14]. The H<sub>2</sub>-TPD curves (Fig. 7) reveal four desorption peaks at around 493, 593, 640, and 822 K obtained for Co-B-0, but only a single intense peak at 593 K and a small shoulder peak at 443 K for Co-B-0.25. Those profiles suggest that Co-B-0.25 contained uniform Co active sites and that the hydrogen adsorption was stronger on Co-B-0.25 than on Co-B-0. The hydrogen atoms strongly adsorbed on Co active sites were favorable for the competitive hydrogenation of C=O against C=C coexisting in CMA molecule [41]. Based on the  $R_{\text{H}}^{\text{m}}$  and reaction time data presented in Table 1, Co-B-0.25 obviously was more active than Co-B-50-30. This also can be attributed to the higher  $S_{\text{Co}}$  and the enhanced intrinsic activity (see  $R_{\text{H}}^{\text{S}}$  values). Meanwhile, Co-B-0.25 was slightly more selective to CMO than Co-B-50-30 (see the CMO yields in Table 1), which also can be attributed to the higher B content in Co-B-0.25.

Table 1 shows the effect of cyclohexane content on the catalytic performance of Co-B samples. The maximum catalytic activity was measured from Co-B-0.25, apparently arising from the  $S_{\text{Co}}$ , because the  $R_{\text{H}}^{\text{S}}$  remained almost unchanged regardless of the cyclohexane content. In accordance with the maximum CMO yields listed in Table 1, Co-B-0.25 was more selective toward CMO than Co-B-0.1 and Co-B-0.2, possibly due to the greater B-content and greater dispersion of the Co-B nanoparticles in the Co-B-0.25 sample. Abrupt decreases in both activity and the selectivity were observed for the Co-B-0.3 sample, likely due to the significant agglomeration of Co-B nanoparticles.

Fig. 8 shows the recycling tests using the Co-B-0 and Co-B-0.25 samples. Significant losses in activity (14%) and CMO selectivity (11%) were observed for Co-B-0 after four recyclings, whereas Co-B-0.25 exhibited a longer lifetime, with activity and selectivity decreasing by only 12% and 3% after seven recyclings. The FTIR spectra of the Co-B-0.25 sample show that the absorbance peaks indicative of polyethylene glycol molecular disappeared completely after being washed, as described in Section 2. Thus, the possible degradation of polyethylene glycol also can be ruled out. Moreover,

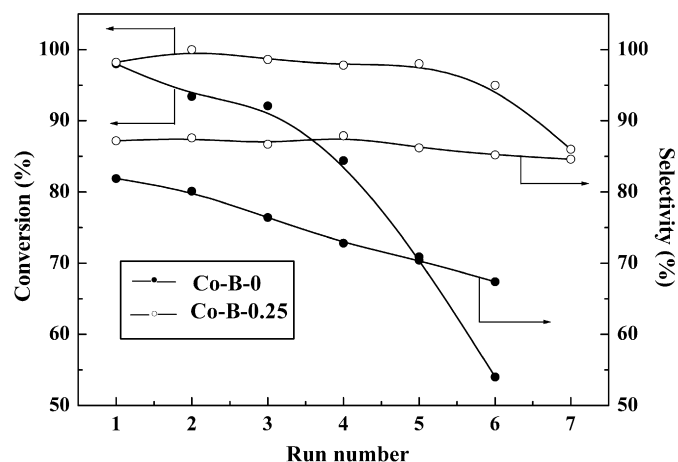


Fig. 8. CMA conversions and CMO selectivity on Co-B-0 and Co-B-0.25 samples as a function of recycling runs. Reaction conditions are given in Table 1.

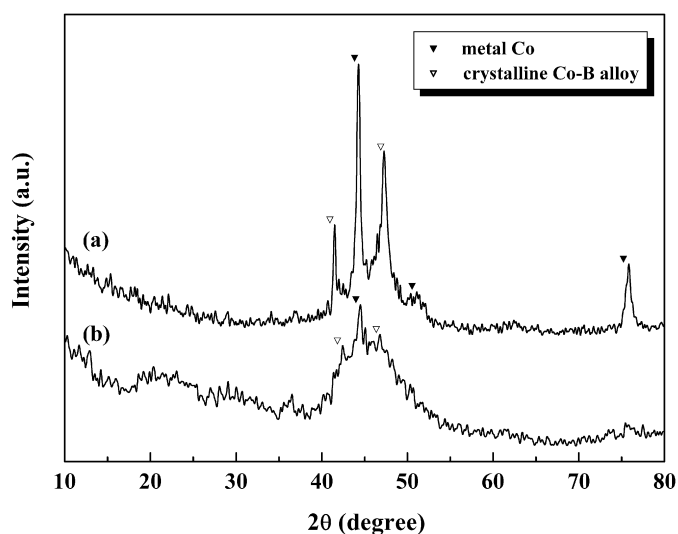


Fig. 9. XRD patterns of (a) Co-B-0 after recycling for 4 times, and (b) Co-B-0.25 after running for 7 times.

ICP analysis reveals that the leaching of Co species was  $<1.0$  ppm, which can rule out the loss of active phases and the advanced reduction of the catalysts. Apparently, partial crystallization occurred for these spent catalysts (Fig. 9), being responsible for the deactivation. On one hand, the crystallization resulted in the decrease of  $S_{Co}$  due to agglomeration of particles [27]; on the other hand, it resulted in transformation from the amorphous structure to the crystalline structure, which was unfavorable for the hydrogenation activity. Meanwhile, the electron density in those electron-enriched Co active sites may have decreased gradually during the crystallization process due to the decomposition of Co-B alloys, leading to the lower CMO selectivity. Co-B-0.25 exhibited better durability than Co-B-0 because of its higher thermal stability, as confirmed by the aforementioned DSC analysis (Fig. 4).

#### 4. Conclusion

In summary, the strategy reported herein provides a facile, one-step, and potentially general procedure for the synthesis of

amorphous alloys with controllable size. The nanoparticles were prepared mainly through chemical reduction of metallic ions with  $BH_4^-$  in the confined voids formed by oil droplets in an oil-in-water microemulsion system. The Co-B sample thus produced demonstrated superior catalytic performance to the regular Co-B during liquid-phase CMA hydrogenation. Our findings demonstrate the advantages of this approach.

#### Acknowledgment

This work was supported by the National Natural Science Foundation of China (20603023), the 863 Project (2007AA03Z339), the Preliminary 973 Project (2005CCA01100), and Shanghai Government (05QMX1442, T0402, 06JC14093, 07dz22303).

#### References

- [1] T.B.L.W. Marinelli, S. Nabuurs, V. Poncet, *J. Catal.* 151 (1995) 431.
- [2] F. Delbecq, P. Sautet, *J. Catal.* 220 (2003) 115.
- [3] Á. Zsigmond, I. Balatoni, K. Bogár, F. Notheisz, F. Joó, *J. Catal.* 227 (2004) 428.
- [4] S.I. Fujita, Y. Sano, B.M. Bhanage, M. Arai, *J. Catal.* 225 (2004) 95.
- [5] A. Ghosh, R. Kumar, *Microporous Mesoporous Mater.* 87 (2005) 33.
- [6] X.Q. Wang, R.Y. Saleh, U.S. Ozkan, *J. Catal.* 231 (2005) 20.
- [7] P. Gallezot, D. Richard, *Catal. Rev.-Sci. Eng.* 40 (1998) 81.
- [8] K. Klement, R.H. Willens, P. Duwez, *Nature* 187 (1960) 869.
- [9] J. Van Wenterghem, S. Mørup, C.J.W. Koch, S.W. Charles, S. Well, *Nature* 322 (1986) 622.
- [10] A. Molnar, G.V. Smith, M. Bartok, *Adv. Catal.* 36 (1989) 329.
- [11] A. Baiker, *Faraday Discuss. Chem. Soc.* 87 (1989) 239.
- [12] Y. Chen, *Catal. Today* 44 (1998) 3.
- [13] J.F. Deng, H.X. Li, W.J. Wang, *Catal. Today* 51 (1999) 113.
- [14] H.X. Li, H. Li, J. Zhang, W.L. Dai, M.H. Qiao, *J. Catal.* 246 (2007) 301.
- [15] H. Bonnemant, R.M. Richards, *Eur. J. Inorg. Chem.* (2001) 2455.
- [16] M.P. Pileni, *J. Phys. Chem.* 97 (1993) 6961.
- [17] M.J. Schwuger, K. Stickdorn, R. Schomäcker, *Chem. Rev.* 95 (1995) 849.
- [18] S. Eriksson, U. Nylén, S. Rojas, M. Boutonnet, *Appl. Catal. A* 265 (2004) 207.
- [19] S.J. Chiang, B.J. Liaw, Y.Z. Chen, *Appl. Catal. A* 319 (2007) 144.
- [20] W.Z. Zhang, X.L. Qiao, J.G. Chen, *Colloids Surf. A* 299 (2007) 22.
- [21] H.X. Li, Y.D. Wu, H.S. Luo, M.H. Wang, Y.P. Xu, *J. Catal.* 214 (2003) 15.
- [22] J.J.F. Scholten, A.P. Pijers, A.M.L. Hustings, *Catal. Rev.-Sci. Eng.* 27 (1985) 151.
- [23] H.X. Li, X.F. Chen, Y.P. Xu, *Appl. Catal. A* 225 (2002) 117.
- [24] H.X. Li, H. Li, W.L. Dai, M.H. Qiao, *Appl. Catal. A* 238 (2003) 119.
- [25] A. Yokoyama, H. Komiya, H. Inoue, T. Masumoto, H.M. Kimura, *J. Catal.* 68 (1981) 355.
- [26] K.S. Martens, J.A. Parton, R. Vercruyse, K. Jacobs, P.A. Maier, *Catal. Lett.* 38 (1996) 209.
- [27] H.X. Li, W.J. Wang, H. Li, J.F. Deng, *J. Catal.* 194 (2000) 211.
- [28] N.S. McIntyre, M.G. Cook, *Anal. Chem.* 47 (1975) 2208.
- [29] H. Li, H.X. Li, W.L. Dai, W.J. Wang, Z.G. Fang, J.F. Deng, *Appl. Surf. Sci.* 152 (1999) 25.
- [30] Z.G. Fang, B.R. Shen, K.N. Fan, *Chinese J. Chem. Phys.* 15 (2002) 17.
- [31] W.L. Dai, H.X. Li, Y. Cao, M.H. Qiao, K.N. Fan, J.F. Deng, *Langmuir* 18 (2002) 9605.
- [32] Y. Nitta, Y. Hiramatsu, T. Imanaka, *J. Catal.* 126 (1990) 235.
- [33] C. Ando, H. Kurokawa, H. Miura, *Appl. Catal. A* 185 (1999) L181.
- [34] B. Liu, L. Lu, T. Cai, K. Iwatani, *Appl. Catal. A* 180 (1999) 105.
- [35] G.D. Angel, J.L. Benitez, *J. Mol. Catal.* 94 (1994) 409.
- [36] G. Blyholder, D. Shihabi, *J. Catal.* 46 (1977) 91.
- [37] H. Noller, W.M. Lin, *J. Catal.* 85 (1984) 25.
- [38] E. Boellaard, R.J. Vreeburg, O.L.J. Gijzeman, J.W. Geus, *J. Mol. Catal.* 92 (1994) 299.
- [39] Y.Z. Chen, S.W. Wei, K.J. Wu, *Appl. Catal. A* 99 (1993) 85.
- [40] Y. Nitta, Y. Hiramatsu, T. Imanaka, *Chem. Express* 4 (1989) 281.
- [41] H.R. Hu, M.H. Qiao, S. Wang, K.N. Fan, H.X. Li, B.N. Zong, X.X. Zhang, *J. Catal.* 221 (2004) 612.